Assessment of protective coatings for metal-supported solid oxide electrolysis cells

Fengyu Shen[a]*, Michael Reisert[b], Ruofan Wang[a], Prabhakar Singh[b], and Michael C. Tucker[a]*

[a]Energy Storage and Distributed Resources Division, Lawrence Berkeley National Laboratory, Berkeley, CA 94720, USA

[b]Department of Materials Science and Engineering, University of Connecticut, Storrs, CT 06269, USA

E-mail: fshen@lbl.gov (F. Shen) mctucker@lbl.gov (M.C. Tucker)

Abstract

Green hydrogen is essential to achieve carbon-neutrality, and solid oxide electrolysis cells can produce hydrogen using renewable power and waste heat. Insufficient long-term durability of solid oxide electrolysis cells has impeded their commercialization. Here, coatings in the porous stainless steel support of metal-support solid oxide electrolysis cells (MS-SOECs) are used to dramatically improve their performance and durability. The long-term degradation rate of uncoated MS-SOECs is highly dependent on the current density, with the fastest degradation occurring at the highest current density tested, 0.5 A cm^{-2}. At this current density, coatings are quite effective. Three protective coatings, Co_3O_4 deposited by atomic layer deposition (ALD), Co_3O_4 deposited by electroplating deposition (ED), and $CuMn_{1.8}O_4$ (CMO) deposited by electrophoretic deposition (EPD), are explored to enhance the performance of MS-SOECs with $La_{0.6}Sr_{0.4}Co_{0.2}Fe_{0.8}O_3$-$Sm_{0.2}Ce_{0.8}O_3$ (LSCF-SDC) as the oxygen catalyst and SDC-Ni as the fuel catalyst. The initial average current density at 1.4 V is increased with coatings. It is 0.83 mA cm^{-2}

for the ALD cells, 1.05 mA cm^{-2} for the ED cells and 1.13 mA cm^{-2} for the EPD cells, compared to 0.65 mA cm^{-2} for the bare cells at 700 °C with 50% H_2 - 50% H_2O. The degradation rate over 1000 h continuous operation is reduced from 36% kh^{-1} to 26% kh^{-1}, 27% kh^{-1}, 19% kh^{-1} with the three coatings, respectively. These improvements are ascribed to reduced Cr poisoning on the oxygen catalyst, which is one of the primary degradation modes for this type of MS-SOEC.

Keyword: Solid oxide electrolysis cell; Hydrogen production; Protective coating; Atomic layer deposition; Electroplate deposition; Electrophoretic deposition

1. Introduction

Hydrogen has high gravimetric energy density and zero carbon dioxide (CO_2) emissions at the point of use, so it recently attracts more attention as an energy carrier as our energy system is transitioning from fossil fuels to low-carbon energy sources.[1] Hydrogen is likely to play a critical role to achieve carbon-neutrality promised by many countries in the coming decades.[2] However, hydrogen does not exist as a natural resource on the Earth, and more than 90% of its current production is from fossil fuels such as natural gas, oil, and coal, with accompanying by-products of carbon monoxide, CO_2 and other greenhouse gases that lead to global warming.[3] Solid oxide electrolysis cells (SOECs) are an attractive technology that convert electrical energy and steam into hydrogen *via* an electrochemical process which has high energy-conversion efficiency, low energy consumption, and the possibility to use high-quality waste heat, while avoiding noble metal-based catalysts.[4] SOECs can store excess electricity to balance the intermittent nature of the renewable sources.[5] Three aspects must be achieved before commercialization: high

performance, high durability for long-term operation, and low cost. A recent study by Shimada et al. exhibited high current density of ~2.3 A cm^{-2} at 1.4 V, 700 °C, and 50% humidity conditions through the use of nanocomposite electrodes.[6] Chen at al. reported a degradation rate of 4.6% kh^{-1} (53 mV kh^{-1}) at 1 A cm^{-2} during 4400 h operation at 800 °C and 90% humidity conditions.[7] This is an impressive demonstration, but the degradation rate is still far higher than the technical target (<4 mV kh^{-1}) proposed by the U.S. Department of Energy. Numerous SOEC degradation modes and mechanisms have been reported. Electrolyte reduction,[8] delamination,[9] intergranular fracture and void formation along the grain boundaries of the electrolyte,[10] have been reported to degrade electrolytes. Microstructural changes and cation interdiffusion,[11, 12] formation of nanoparticle clusters,[13] phase change,[14] SrO segregation on the surface,[15] and contaminants from iron-chromium (Fe-Cr) stainless steel,[16] have been reported to degrade perovskite oxygen electrodes. Microstructure instability,[17] agglomeration,[18] and Ni coarsening,[18] have been reported to degrade Ni-based fuel electrodes.

Metal-supported solid oxide cells (MS-SOCs) with symmetric backbones can endure severe thermal and mechanical stresses and redox phenomena during operation.[19] They incorporate a porous ferritic stainless steel as a substrate and are suitable with intermittent operations due to their unique advantages of good redox stability and excellent thermal cycling resistance.[19, 20] Compared with conventional all-ceramic solid oxide cells, the material cost of MS-SOCs is lower, as 90 vol.% of the cell is stainless steel metal support. Metal-supported solid oxide fuel cells (MS-SOFCs) are well-developed, and during the previous decade many research groups have begun optimizing and demonstrating metal-supported solid oxide electrolysis cells (MS-SOECs).[21] Our previous MS-SOEC study reported a current density of 0.6 A cm^2 at 1.4 V, 700 °C, and 50%

humidity conditions, using $La_{0.6}Sr_{0.4}Co_{0.2}Fe_{0.8}O_3$-$Sm_{0.2}Ce_{0.8}O_3$ (LSCF-SDC) as the oxygen evolution catalyst and SDC-Ni as the steam reduction catalyst.[22] After 1000 h continuous operation resulting in a degradation rate of 16% kh^{-1} at 0.33 A cm^{-2}, post-mortem analysis demonstrated two primary degradation modes: Cr poisoning on the oxygen electrode catalyst, and fuel electrode catalyst coarsening. Oxidation of the metal support and local elemental accumulation of Ni were detected as secondary degradation modes.

Despite the excellent activity of LSCF, Cr poisoning is one of the major issues when using Cr-containing stainless steel as interconnects or other components. LSCF is a perovskite ceramic, with an electronic conductivity of 257 to 412 S cm^{-1} between 450 and 900 °C.[23] It is widely used for intermediate temperature SOFCs due to its mixed ionic and electronic conductivity and oxygen reduction reaction catalytic activity.[24] However, Cr vapor species, such as CrO_3 and $CrO_2(OH)_2$, react with LSCF and form $SrCrO_4$, leading to an increase of ohmic resistance and polarization resistance.[12, 25] For the porous metal supports used here, the growth of the chromia oxidation layer in air atmosphere is a source of Cr vapor species.[26] To prevent Cr poisoning, extensive efforts have been devoted to develop mitigation strategies including discovery of Cr-tolerant catalysts and Cr-getter materials. Perhaps the most successful strategy is the use of protective coatings to inhibit Cr diffusion outward from stainless steel.[27] Spinel $CuMn_{1.8}O_4$ (CMO) coating or its variant has been demonstrated as a particularly effective coating composition.[28, 29] Our previous work extended the coating concept by applying a coating throughout the oxygen-side porous stainless steel support of a MS-SOFC. The degradation rate was reduced to 2.3% kh^{-1} with a thin Co_3O_4 coating deposited by ALD.[30]

In this work, the use of coatings to mitigate Cr migration is extended to MS-SOECs. Three coatings were adopted: nanoscale Co_3O_4 deposited by atomic layer deposition (ALD), microscale Co_3O_4 prepared by electroplating deposition (ED), and CMO formed by electrophoretic deposition (EPD) of particles. Enhanced initial performance and long-term durability were demonstrated for the cells with these coatings, compared to bare uncoated cells. Co inter-diffusion with the outer oxide is observed for the ALD coating. Cr accumulation was detected on the surface of the ED coating after 1000 h operation. In contrast, the EPD coating did not react with the Cr species from the metal support during the long-term test. Thus, the EPD coating is the most effective one for inhibition of Cr diffusion.

2. Experimental

2.1. Cell fabrication

The symmetric MS-SOEC includes a thin ceramic electrolyte and scaffold electrode backbone layers (ScSZ, DKKK), and low-cost ferritic stainless steel supports (P434L, Ametek). The composition of P434L is listed in Table 1. A detailed cell fabrication procedure can be found in our previous work.[22] Briefly, each layer was prepared by tape casting. Polymethyl methacrylate (PMMA) pore former beads (Esprix Technologies, USA) were used as a pore former in metal supports and electrodes. After drying, these layers were then laminated at 75 °C to form a symmetric cell architecture. Cells were laser cut and debinded at 525 °C for 1 h in air and then sintered at 1350 °C for 2 h in a tube furnace with 2% H_2-Ar atmosphere. The sintered cells were 27 mm diameter with 5 cm^2 total active area (infiltrated with catalysts and not covered by sealing

glass). The 3D reconstruction image in Figure S1 shows the dense electrolyte is ~10 µm, and the ceramic backbone layer is 20-30 µm. The backbone includes micron-scale large pores and submicron-scale small pores, which can serve as triple phase boundaries. The metal support is the thickest component in the cell, ~250 µm, providing mechanical support and serving as current collectors. The porosities of the metal support and backbone are approximately 46% and 42%, respectively. The adequate porosity of the metal and ceramic layers enables catalyst infiltration throughout the cell structure without catalyst clogging, and without sacrificing the cell's mechanical ruggedness.

Table 1. Composition of P434L stainless steel (Ametek Specialty Metal Products).

Element	Fe	Cr	Mo	Si	Mn	P	C	S
Conc. (%)	Bal.	16.66	0.94	0.85	0.14	0.016	0.012	0.006

2.2. Deposition of the coatings

All reagents were purchased from Sigma-Aldrich, USA, unless noted.

2.2.1. Atomic layer deposition

Co_3O_4 coating was implemented by ALD (Oxford FlexAL, Oxford Instruments, UK) on the oxygen electrode side of MS-SOECs. The cells were pre-oxidized at 750 °C for 10 h in air and placed on a Si wafer with the edges of cells covered by Kapton tape, ensuring only the top side of cells was coated. Bis(cyclopentadienyl)cobalt(II) was used as the organometallic precursors, and deionized water as the oxygen source. The coating was conducted at 60 °C with 350 cycles.

2.2.2. Electroplating deposition

Co metal layer was deposited on the metal support of the oxygen side by ED. The solution was prepared with 0.751 g $CoSO_4 \cdot 6H_2O$, 0.143 g $CoCl_2 \cdot 6H_2O$ and 0.056 g H_3BO_3 in 100 mL deionized water. The pH of the solution was adjusted to 3.6 by adding HCl. A Pt mesh was spot-welded on one side of the cell and connected to the negative lead of a power supply (VSP-300, BioLogic, France). A Co plate was connected to the positive lead, as a counter electrode. A constant current density of 4 mA/cm^2 was applied for 10 min. The coated cells were oxidized at 800 °C in air for 5 h to convert Co to Co_3O_4.

2.2.3. Electrophoretic deposition

CMO powder was synthesized by a sol-gel method.[28, 31] Briefly, 3.081 g $Cu(NO_3)_2 \cdot 2.5H_2O$, 5.984 g $Mn(NO_3)_2 \cdot 4H_2O$, 1.754 g glycine and 15 mL deionized water were mixed in a stainless steel beaker. The reagents were completely dissolved with magnetic stirring. The hot plate temperature was raised to 100 °C for 25 min to evaporate the solvent, then raised to 300 °C until auto-combustion occurred. The resulting powder was calcined at 800 °C for 2 h to fully react the components. Then, 1.8 g synthesized CMO powder was ball milled with 15 mL ethanol for 24 h and then 150 mL acetone was added. The suspension was sonicated before adding 0.86 mL of 1 M iodine in ethanol, followed by another sonication. The suspension sat for 30 min before starting the EPD process. A Pt mesh was spot-welded on one side of a cell and connected to the negative terminal of a power source. A Cu plate was connected the positive terminal as a counter electrode. Both were submerged in the suspension. A constant voltage of 20 V was applied for 10 min. The coated cells

were thermally treated at 1000 °C for 4h in 2% H_2 atmosphere, then at 750 °C for 5 h in air to convert the CMO particles into an adherent coating.

2.3. Catalyst infiltration

Electrode catalysts were introduced by infiltration under vacuum, following a fast firing procedure. Bare cells were pre-oxidized at 850 °C for 10 h before catalyst infiltration. Stoichiometric nitrate salts, as the precursors of cations, were dissolved in water with Triton-X 100 surfactant. Typically for the oxygen catalyst, 5.078 g $La(NO_3)_3{\cdot}6H_2O$, 1.655 g $Sr(NO_3)_2$, 1.198 g $Co(NO_3)_2{\cdot}6H_2O$ and 6.649 g $Fe(NO_3)_3{\cdot}9H_2O$ were dissolved in a 9 g mixture of water and Triton-X 100 at room temperature to prepare LSCF. Then, 1.966 g $Sm(NO_3)_3{\cdot}6H_2O$ and 7.681 g $Ce(NO_3)_3{\cdot}6H_2O$ were dissolved in a 3.2 g mixture of water and Triton X-100 at room temperature to prepare $Sm_{0.2}Ce_{0.8}O_3$ (SDC). For the fuel catalyst, 0.569 g $Sm(NO_3)_3{\cdot}6H_2O$, 2.225 g $Ce(NO_3)_3{\cdot}6H_2O$ and 4.567 g $Ni(NO_3)_2{\cdot}6H_2O$ were dissolved in a 3.2 g mixture of water and Triton-X 100 to prepare the SDC and NiO. The volume ratio of SDC to Ni was 60:40 (denoted as SDCN40). Three drops of the aforementioned LSCF solution were cast on the oxygen electrode and infiltrated under vacuum, then the cell was dried at 90 °C for 20 min. The cell was flipped over and infiltrated with SDCN40 solution with the same procedure. After drying, the cell was directly loaded into a pre-heated furnace (800 °C) and unloaded after 30 min.[32] Both catalysts were fired during this process. LSCF solution was replaced by SDC solution on the second cycle. The cell was alternately infiltrated with LSCF and SDC solution for 11 cycles. A total of 6 LSCF, 5 SDC, and 11 SDCN infiltration cycles were applied.

2.4. Cell assembly and test

Cells were sealed on stainless steel test rigs with glass sealant for testing. After catalyst infiltration, a Pt mesh was spot-welded on the fuel electrode side of the cell and two Pt wires were spot-welded on the mesh for electrical connection. The cell was then mounted on a 410 stainless steel test rig using glass paste which was prepared with 80 wt.% glass powder (GM31107, Schott, Germany) and 20 wt.% glass ink vehicle (Fuel Cell Materials, USA). The cell was then heated to 200 °C at 2 °C min^{-1} and then to 700 °C at 10 °C min^{-1} with 1 h seal curing. A second round of glass paste loading was conducted after a Pt mesh and two Pt wires were spot-welded onto the oxygen electrode side. After curing the glass paste with the same procedure, the chamber of the test rig was flushed with nitrogen, and hydrogen was then bubbled through a water bath at a flow rate of 75 cm^3 min^{-1}. The NiO on the fuel electrode side was completely reduced to Ni metal when the open circuit voltage (OCV) of the cell was stabilized at ~1.12 V. Hydrogen was used as the carrier gas in the fuel electrode, and the steam content was controlled to 50% by adjusting the temperature of the water bath to 82 °C. The fuel tubing from the bubbler to the test rig was wrapped with heating tape to prevent condensation. During the cell testing, the oxygen electrode was always exposed to static ambient air.

The cells were tested at 700 °C under electrolysis mode. For the I-V curve measurement, potentiodynamic scans starting from OCV to the electrolysis (positive) direction were performed, at a voltage scan rate of 10 mV s^{-1}. Electrochemical impedance spectroscopy (EIS) measurements were performed in the frequency range from 200 kHz to 100 mHz with a sinus amplitude of 5 mV, at OCV. All electrochemical measurements were conducted with a multichannel potentio/galvanostat (VMP3, BioLogic, France) equipped with power boosters (VMP3B-5, BioLogic, France).

2.5. Chromium transpiration measurement

Cr evaporation from the bare, ALD coated, and EPD coated cells without catalyst infiltration was measured using a Cr transpiration test setup and the details can be found elsewhere.[26] Briefly, a quartz tube, designed with a capillary opening to prevent the back diffusion of the vapor species, was used to conduct the experiment. Experimental test conditions simulated SOEC anodic atmosphere of 3% H_2O/97% air at 700 °C. The deposited Cr on the quartz tube, elbow and the condenser was extracted by dissolving it in aqueous 20% HNO_3. Any undissolved Cr species were further removed from the glass wall by dissolving in alkaline potassium permanganate (0.3% $KMnO_4$ in 1% NaOH, upon heating at 90 °C), ensuring the conversion of the remaining Cr species from Cr^{3+} to Cr^{6+}. Inductively coupled plasma-optical emission spectroscopy (ICP-OES, 7300 DV, PerkinElmer, USA) was performed to analyze the Cr concentration and calculate the total Cr evaporation rate. The final concentrations of Cr were averaged from 3 separate samples.

2.6. Characterization

The morphology of the coatings and catalysts was imaged using a field-emission scanning electron microscope (FESEM, Zeiss Gemini Ultra-55, Germany) with an energy dispersive X-ray spectroscopy (EDS) detector. Crystal structures were characterized by X-ray diffraction (XRD, D5005, Bruker, Germany) using a Cu Kα x-ray source over a 2θ range of 20-80°. Microtomography was conducted at the Advanced Light Source (ALS) Beamline 8.3.2 at Lawrence Berkeley National Laboratory, with pixel size of 0.65 µm. Images were collected over 180° in 0.072° steps, with 24 keV X-ray. The 3D reconstructions were performed with TomoPy, and visualization and image were analyzed with Avizo software. Cross-sections of select sample surface regions were

prepared using focused ion-beam (FIB, Helios Nanolab 460F1 DualBeam, ThermoFisher Scientific, USA) milling with a Ga ion source and analyzed using transmission electron microscopy (TEM, Talos F200X G2, ThermoFisher Scientific, USA).

3. Results and discussion

The morphology and Cr-barrier performance of the coatings was characterized. Then, cells with and without coatings were operated in SOEC mode for 1000 h. Finally, post-mortem analysis determined the degradation modes and demonstrated that the coatings indeed suppress Cr migration from the stainless steel support to the LSCF catalyst.

3.1. Coating characterization

Both pre-oxidation and the deposition of coatings provide relatively uniform surface layers on the stainless steel support. The surface scale of the pre-oxidized metal support is composed of smaller chromia and larger Cr-Mn oxide grains (Figures 1a). The surface of the ALD coating is uniform and dense (Figure 1b). The feature size is as small as 100 nm. Although the ALD coating is thin, the metal support surface is uniformly coated. The surface of the ED coating is also uniform and dense, with a feature size of 100-500 nm that is larger than the ALD coating (Figure 1c). EDS was conducted on the surface of the coating (Figure S2a). Cr and Fe are detected and can be ascribed to the small coating thickness (~ 2 μm) and the reaction between the Co_3O_4 coating and Cr species at the interface between the coating and stainless steel. The EPD coating morphology is different from the other coatings (Figures 1d and S3). Porosity is visible on the surface, and the coating penetrates throughout the porous stainless steel support, consistent

with previous studies.[29, 31, 33] The grain size is around 500 nm. The surface of the coating contains a very small amount of Cr and no Fe, due to the thick coating layer (6-10 µm) at the surface and minimal Cr reaction with the coating during the thermal treatment (EDS shown in Figure S2b). The atomic ratio of Cu to Mn is 1:1.53, which is Cu-rich compared to the prepared powder composition with Cu to Mn ratio of 1:1.8. Presumably, this is because the Cu plate used as the counter electrode is partially stripped and the resulting Cu ions are electroplated on the cell. Note that in all cases, the infiltrated catalysts (applied after the coatings are deposited) also coat the interior surface of the stainless steel support. Although the catalysts are porous, they do offer some protection from oxidation and reduction of Cr evaporation at 700°C.[26] Nevertheless, the coatings studied here are intended to reduce the Cr evaporation much more than the infiltrated catalyst layer.

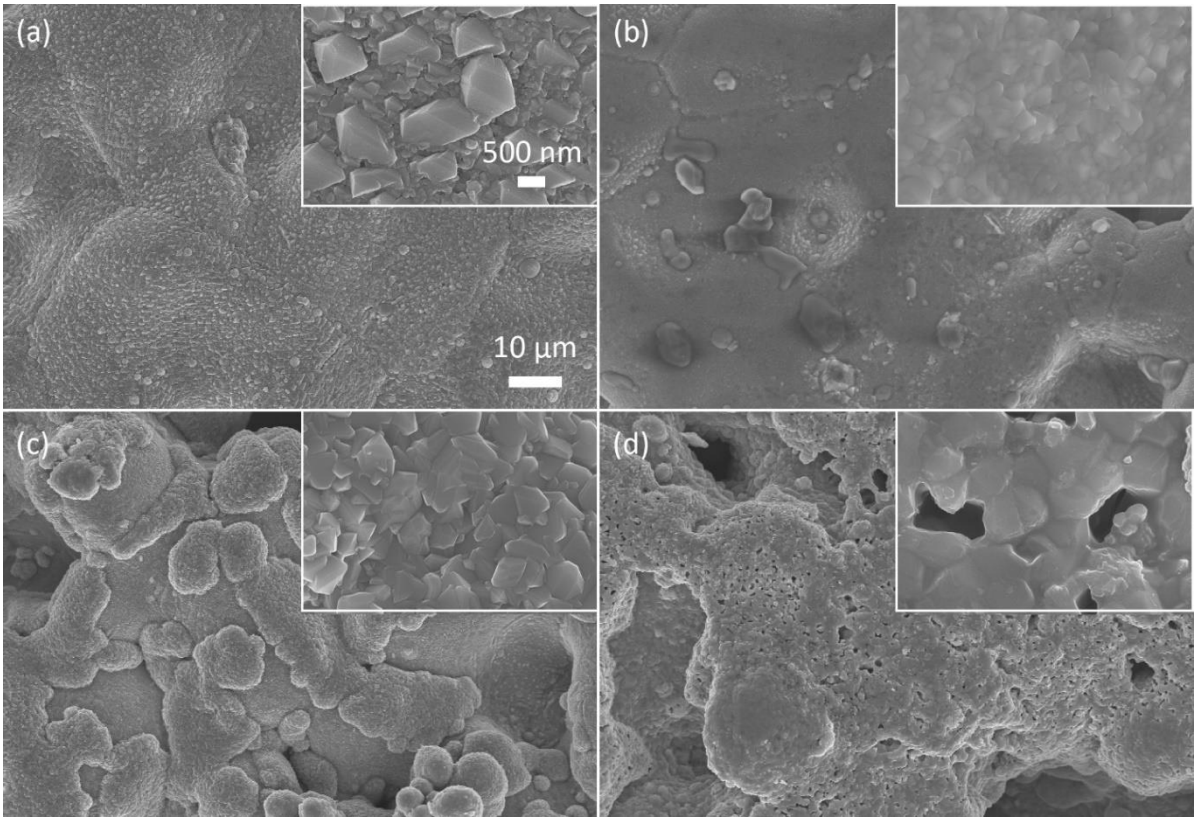

Figure 1. **Coating morphology.** SEM images of the top surface of the metal support with (a) no, (b) ALD, (c) ED, and (d) EPD coatings.

Cr transpiration analysis directly demonstrates the effectiveness of the coatings, especially the EPD coating, for inhibiting Cr evaporation. Bare and coated samples without infiltrated catalysts were oxidized in humidified air for 500 h, and the evaporated Cr was collected for analysis. The Cr evaporation rate for the bare support is 1.75×10^{-11} kg m^{-2} s^{-1}. The ALD coating reduces the rate by more than 50%, to 8.22×10^{-12} kg m^{-2} s^{-1}. The impact of the very thin but dense ALD coating is similar to the effect of a thick but porous LSCF-SDC infiltrated layer, which reduces the rate to 7.13×10^{-12} kg m^{-2} s^{-1}.[26] The Cr evaporation rate for the support with the EPD coating was limited to 1.43×10^{-13} kg m^{-2} s^{-1}, which is two orders of magnitude lower than the bare cell and one order of magnitude lower than the ALD coated cell, highlighting the efficacy of the EPD coating in mitigating Cr evaporation. The XRD patterns of the EPD-coated metal support before and after the 500 h Cr transpiration test are compared in Figure S4. Major peaks correspond to the spinel $CuMn_{1.8}O_4$ coating. These peaks overlap with peaks from $CrCuMnO_4$, Cr-substituted $CuMn_{1.8}O_4$, possibly formed during Cr transpiration. However, the section below demonstrates there is no obvious Cr in the EPD coating even after the 1000 h test, which supports that the chemistry of the coating has not changed after the Cr transpiration experiment. Minor peaks correspond to the base alloy and some Si-based oxides (P434L alloy contains 0.85% Si). It is likely that Si-based oxides are incorporated in the EPD coating during the coating process and subsequent operation. The major peaks before and after the Cr transpiration experiment are the same, demonstrating the stability of the EPD coating.

In contrast, the ALD coating is unstable and diffuses into the oxide scale on the stainless steel. Samples with the ALD coating were analyzed by FIB/TEM before and after transpiration. A small piece with the porous structures from each sample was lifted out by FIB. Before transpiration, a Co oxide layer with the thickness of 30-40 nm coated the metal support, as shown by EDS mapping (Figure 2a). The sample was pre-oxidized before the ALD coating, and a ~500 nm thick chromia scale grew on the metal support with large grains of $MnCr_2O_4$ above the chromia. There is also a thin SiO_2 sub-scale (<50 nm) below the chromia scale, which was formed during the pre-oxidization process. As expected, the chromia, $MnCr_2O_4$, and SiO_2 scales continue growing during the Cr transpiration experiment due to continued oxidation of the stainless steel. After 500 h Cr transpiration (Figure 2b), the continuous Co layer is no longer visible. Co diffused throughout the scale and preferentially segregated to the $MnCr_2O_4$ spinel grains. The ALD coating is not stable during the 500 h thermal treatment, and is therefore expected to be similarly unstable during SOEC operation at similar conditions. This may explain the poor performance of the ALD coating, discussed below.

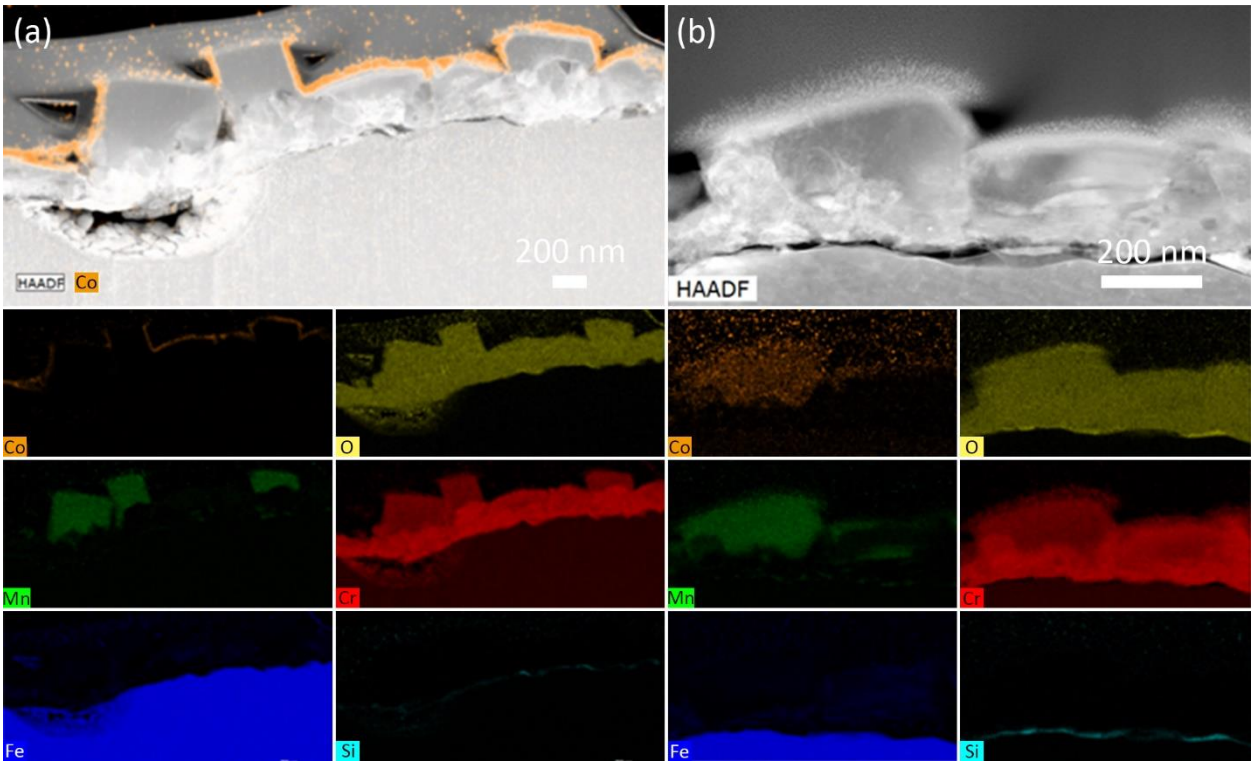

Figure 2. Instability of the Co ALD coating. TEM-EDS of the pre (a) and post (b) transpiration measurement for the metal supports without catalyst infiltration.

3.2. Electrochemical testing

Before the performance of the coatings was evaluated, baseline bare cells were operated with different current densities and the durability is shown in Figure 3. The OCV of the cells at 700 °C with 50% H_2-50% H_2O on the fuel electrode is ~0.97 V. The initial polarization resistance calculated as the difference between OCV and operating voltage is 0.65 to 0.85 Ω cm^2. The degradation rate increases with higher current density. After 1000 h test at 700 °C, the cumulative degradation rates are 12, 21 and 36% kh^{-1}, for current density of 0.2, 0.33 and 0.5 A

cm^{-2}, respectively. Based on these results, the most aggressive condition (0.5 A cm^{-2}) was selected for further testing with coatings.

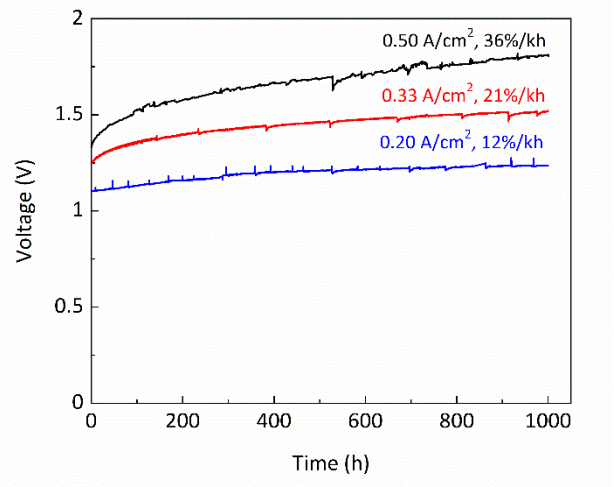

Figure 3. Durability of bare cells. Galvanostatic operation at various current densities at 700 °C with 50% H_2-50% H_2O.

The coatings dramatically improve the initial electrolysis performance compared to the bare cell, as shown in Figure 4a. At a cell voltage of 1.4 V, the current density is 0.68 A cm^{-2} for the bare cell, which is consistent with our previous study with a slow catalyst firing procedure.[22] The current density is improved to 0.86 A cm^{-2} with the ALD coating, 1.14 A cm^{-2} with the ED coating, and 1.19 A cm^{-2} with the EPD coating. These current densities are from the best-performing cell tested for each type. The performance of all cells tested is shown in Figure S5 and Table S1. The average current density at 1.4 V is 0.65±0.03 A cm^{-2} for bare cells, 0.83±0.03 A cm^{-2} for the ALD coated cells, 1.05±0.06 A cm^{-2} for the ED coated cells and 1.13±0.05 A cm^{-2} for the EPD coated

cells. The performance for each type of cell is reproducible and the cell-to-cell variation is significantly smaller than the variation between coating types.

EIS spectra of all cells were obtained before beginning long-term operation (Figure 4b). The ohmic resistance is 0.42, 0.30, 0.23 and 0.27 Ω cm^{-2} for the bare, ALD, ED, EPD coated cells, respectively. All of the coatings decreased the ohmic impedance by more than 30% compared to the bare cell baseline, which is ascribed to less oxidization of the metal support and less Cr reaction with the oxygen catalyst. The polarization resistance is 0.36, 0.38, 0.29 and 0.20 Ω cm^{-2} for the bare, ALD, ED, and EPD coated cells, respectively. The ALD coating does not decrease the polarization resistance while the ED and EPD coatings decrease it by 20 and 44%, respectively. The coatings beneficial impact on performance is thought to be due to blocking of Cr migration from the metal support to the active oxygen catalyst sites as discussed below in Section 3.3. Therefore, less poisoning of the catalyst occurs during cell fabrication, maintaining higher conductivity and catalytic activity compared to reaction products of LSCF and Cr.[34] This contributes to the lower ohmic and polarization impedances with the coatings. The ALD coating was deposited on the porous electrode as well as the metal support, possibly acting as an ion blocking layer or reacting with the electrocatalyst. Moreover, the thicker ED coating and less Cr-reactive EPD coating are more effective than the ALD coating and less Cr diffused to poison the LSCF catalyst during fabrication. Thus, the ALD coating is not as effective to lower the polarization resistance, compared to the other two coatings. After 1000 h operation, the current density decreases to 0.27, 0.30, 0.40 and 0.47 A cm^{-2} at a cell voltage of 1.4 V for the bare, ALD, ED and EPD coated cells, respectively (Figure 4c), which are 35 to 40% of the initial current densities. The ohmic resistance is 0.71, 0.63, 0.63 and 0.42 Ω cm^{-2} for the bare, ALD, ED, and EPD coated cells,

respectively (Figure 4d). The polarization resistance is 1.34, 1.00, 0.85 and 0.71 Ω cm^{-2} for the bare, ALD, ED, and EPD coated cells, respectively. For the bare cell, the ohmic and polarization resistances increase a similar amount, while for the coated cells, the ohmic resistance increases more than the polarization resistance. This is consistent with the ohmic increase during operation being dominated by catalyst coarsening, which is not impacted by the coatings, whereas the polarization increase is dominated by Cr migration which is highly impacted by the coatings as discussed below in Section 3.3.

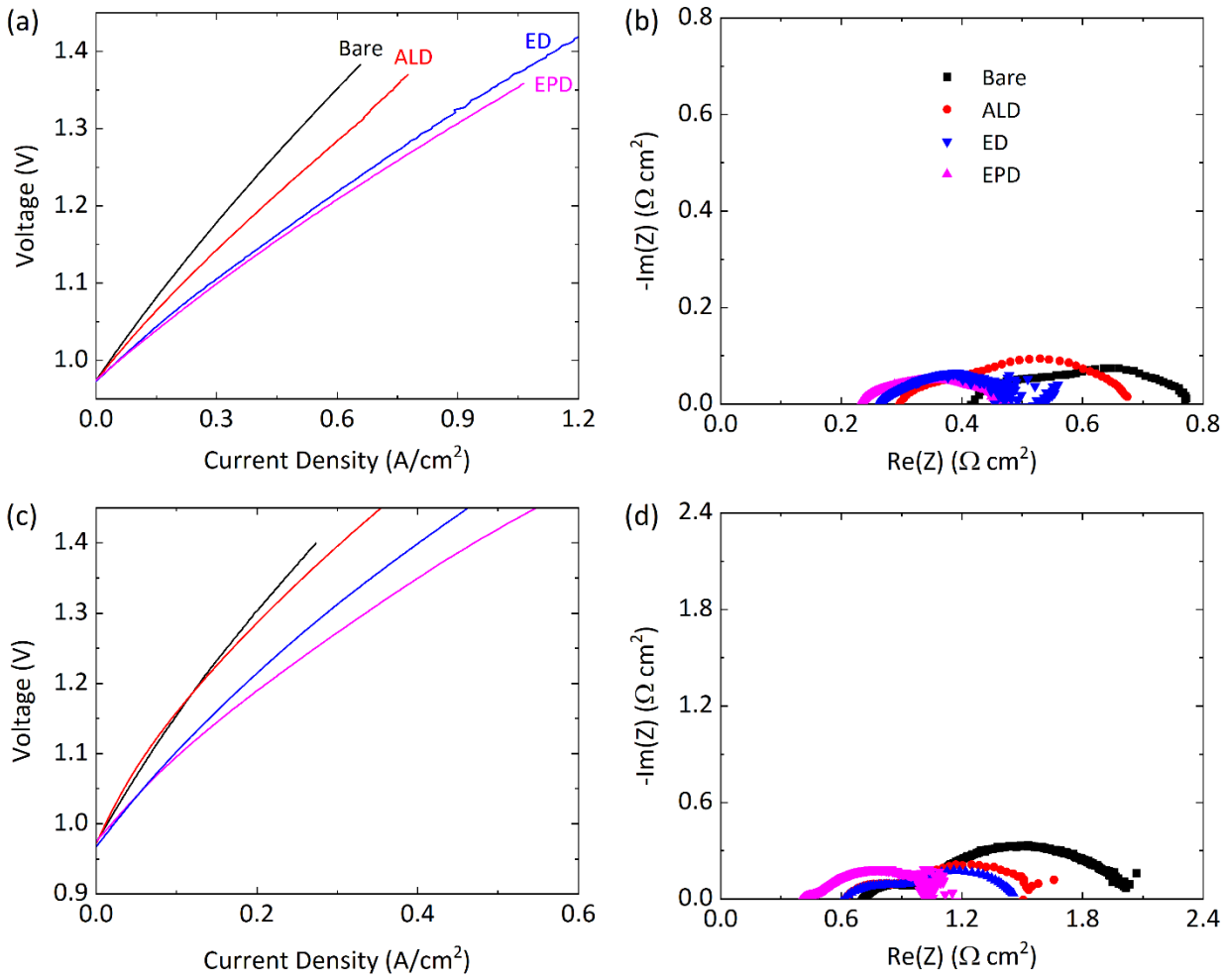

Figure 4. **MS-SOEC initial performance.** (a) (c) I-V curves and (b) (d) EIS at OCV of the bare and coated cells at 700 °C with 50% H_2-50% H_2O. (a) (b) before and (c) (d) after 1000 h operation.

The coatings significantly reduce degradation of the cell performance. The long-term durability of the bare and coated cells was compared at a constant current density of 0.5 A cm^{-2} (Figure 5). All the cells were tested at the same conditions. The initial voltage of the cells with the ED and EPD coatings was similar, and lower than that of the ALD cell and bare cell. This is consistent with the initial I-V polarization (Figure 4a). For the bare cell, the average cell voltage degradation rate over 1000 h operation was 36% kh^{-1}. Rapid degradation (75% kh^{-1}) was observed during the initial 300 h. After this initial transient period, the degradation rate was slower and more consistent at an average rate of 16% kh^{-1} from 300 to 1000 h (Table 2). The cell with the ALD coating degraded 26% in 1000 h. Similarly to the bare cell, it degraded more slowly after an initial transient period (50% kh^{-1} in 300 h), at a degradation rate of 14% kh^{-1} between 300 h and 1000 h. The cell with the ED coating degraded 27% in 1000 h, similar to the cell with the ALD coating, however the initial transient period (42% kh^{-1} in 300 h) was less pronounced and the degradation rate between 300 h and 1000 h was higher (18% kh^{-1}). These two Co_3O_4 coatings do not enhance durability much during 1000 h operation, regardless of the coating thickness or deposition method. This is ascribed to the reaction between the Co_3O_4 coatings and Cr species discussed below in Section 3.3. The cell with the EPD coating shows the best durability, with an average degradation rate of 19% kh^{-1} during 1000 h operation, 30% kh^{-1} in 300 h operation and 13% kh^{-1} between 300 h and 1000 h.

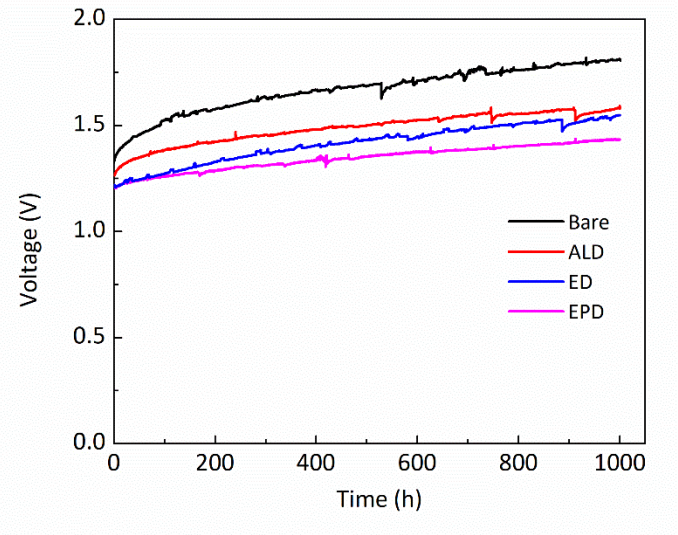

Figure 5. Coatings improve durability. Galvanostatic operation of bare and coated cells at 0.5 A cm^{-2} constant current and 700 °C with 50% H_2 - 50% H_2O.

Table 2. **Impact of coatings on performance and durability.** Initial ASR calculated from the difference between operating voltage and OCV, and degradation rates for 0-1000 h, 0-300 h and 300-1000 h.

Cells	Initial ASR (Ω cm^2)	Degradation rate (% kh^{-1})		
		0-1000 h	0-300 h	300-1000 h
Bare	0.65	36	75	16
ALD	0.51	26	50	14
ED	0.39	27	42	18
EPD	0.37	19	30	13

3.3. Post-mortem analysis

After fabrication and operation, cells were analyzed to determine the impact of Cr migration, fuel catalyst coarsening, and other degradation modes. Cr poisoning of the oxygen catalyst was previously determined to be a primary degradation mode for bare cells.[22] In response, the coatings in this study are intended to inhibit the Cr diffusion from the stainless steel support to the catalyst in the electrode. Direct evidence of the effectiveness of the coatings for mitigating Cr migration is provided in Figure 6. The Cr concentration in the oxygen catalyst was determined with SEM/EDS after fabrication and after 1000 h operation. Cell fabrication promotes Cr migration to the oxygen catalyst during the infiltration process, where the cell is held at 800 °C for 30 min in air 11 times. While this is a relatively short cumulative exposure, it is considered to be more aggressive than a similar time period of long-term operation at 700 °C due to the higher temperature. For the bare cell, the ratio of Cr/La is 0.17 for the fresh cell, indicating significant Cr migration during fabrication. The ratio increases to 0.60 after the durability test. All of the coatings reduce the Cr migration during fabrication and subsequent operation, and the EPD coating is substantially more effective than the others and provides a three-fold reduction in total Cr accumulation compared to the bare cell. The ratio of Cr/La increases from 0.14 to 0.40 for the cell with the ALD coating, from 0.09 to 0.39 for the cell with the ED coating, and from 0.06 to 0.21 for the cell with the EPD coating. The Cr concentration with the ED coating is lower than with the ALD coating for fresh cells, but it is almost the same for both cells after 1000 h test. This is consistent with their durability performance (Figure 5). The Cr concentration increased after 1000 h operation for all of the cells. The overpotential is almost linearly correlated to the ratio of Cr/La for the cells before and after 1000 h, indicating that Cr content is a dominant factor for the

cell degradation (Figure S6). These coatings, including the best-performing EPD coating, cannot completely inhibit Cr diffusion. Therefore, further effort to optimize the composition, densification, and thickness of the coatings is expected to be fruitful.

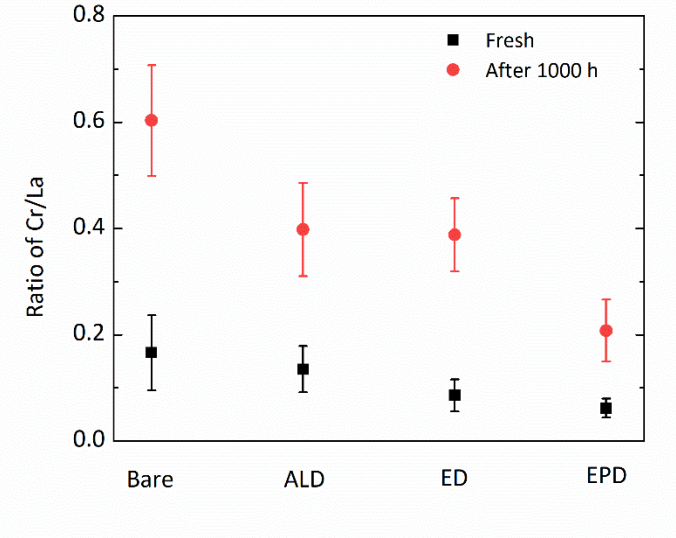

Figure 6. **Cr accumulation in the electrode.** Ratios of Cr to La in the LSCF-SDC catalyst for the bare and coated cells, after cell fabrication (squares) and after 1000 h operation (circles).

The morphology and composition of the ED and EPD coatings after 1000 h operation were analyzed with SEM/EDS (Figure 7). The ALD coating is not shown here because it is too thin to image with SEM. The ED coating appears dense and the EPD coating contains some pores but they do not appear to be interconnected. The line scan for the ED coating shows that Co did not diffuse into the metal support and Cr and Mn accumulated between the metal support and the coating, presumably due to oxidation of the stainless steel. Significant diffusion of Mn into the Co coating was not observed. Moreover, Cr diffused outward and accumulated on the surface of the coating. Cr and Mn overlap at the interface, which could form common (Cr,Mn) compounds.

In contrast, for the EPD coating, there is only Cr accumulation between the metal support and the coating. No Cr is observed in the coating or on the coating surface. This is consistent with the better Cr-blocking performance of the EPD coating (Figure 6). For the EPD coating, the distribution of Mn and Cu is uniform, suggesting there is no phase separation for the coating during operation. Note that P434L stainless steel contains Mn, which is detected by EDS. These observations confirm that the EPD coating is more effective than the ED coating for inhibiting Cr diffusion outward from the stainless steel.

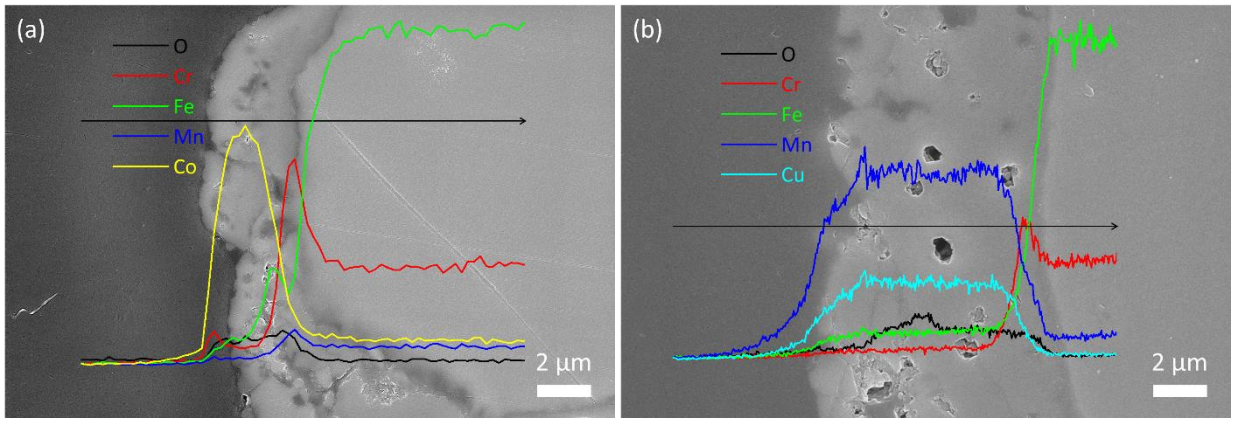

Figure 7. **Coating composition after operation.** EDS line scan along the cross section of the (a) ED and (b) EPD coated metal supports after 1000 h operation. Arrows indicate the EDS scan lines.

Fuel catalyst coarsening appears to be a primary degradation mode for all cells, but the LSCF-SDC oxygen catalyst did not coarsen for the bare or coated cells, consistent with our previous results for bare cells at lower current density.[22] The LSCF-SDC particle size remains 20 to 30 nm after

1000 h operation (Figure S7). The fuel catalyst coarsened from < 20 nm to > 50 nm after 1000 h test, for all bare or coated cells (Figure S8). Preventing the fuel catalyst coarsening would further enhance the durability of the MS-SOECs.

4. Conclusions

MS-SOECs with and without coatings on the oxygen side support are operated for 1000 h. The degradation of bare cells is highly dependent on the applied current density, with higher current density leading to faster degradation. Three coatings are used to inhibit Cr diffusion, to address Cr poisoning of the oxygen catalyst which is a primary degradation mode. The Co_3O_4 ALD and CMO EPD coatings reduce Cr transpiration by 50% and 80%, respectively. All the coatings improve the initial current density at 1.4 V and provide higher durability during 1000 h operation. The current density at 1.4 V for the cells with the EPD coating is as high as 1.13 A cm^{-2}, which is among the best performance reported for a MS-SOEC with stainless steel support and zirconia electrolyte. The Co_3O_4 coatings are less effective than the EPD coating regardless of their thickness, as they react with Cr species during long-term operation. TEM/EDS demonstrates Co deposited by ALD preferentially segregates at the spinel $MnCr_2O_4$ surface. Also, Cr accumulation on the surface of the ED coating is confirmed after 1000 h test, further demonstrating the reaction. Overall, EPD coating, the best of the candidates studied, is stable and effective to suppress Cr diffusion outward from the stainless steel.

Supporting information

3D structure, cross section SEM of a cell with EPD coating, compositions of ED and EPD coatings, XRD patterns of the EPD coated metal support before and after 500 h Cr transpiration test, reproducibility of I-V performance, correlation of overpotential and ratio of Cr/La, oxygen and fuel catalyst morphology, current densities at 1.4 V for all the tested cells

Acknowledgments

The authors gratefully acknowledge research support from the HydroGEN Advanced Water Splitting Materials Consortium, established as part of the Energy Materials Network under the U.S. Department of Energy, Office of Energy Efficiency and Renewable Energy, Fuel Cell Technologies Office, under Contract Number DE-AC02-05CH11231. The use of Zeiss Gemini Ultra-55 FESEM in the Molecular Foundry and resources in the Advanced Light Source (ALS) of Lawrence Berkeley National Laboratory was supported by the Office of Science, Office of Basic Energy Sciences, of the U.S. Department of Energy under Contract No. DE-AC02-05CH11231. We are grateful to Dr. Dilworth Parkinson for help with micro-tomography measurement at Beamline 8.3.2 of ALS. Drs. Lichun Zhang and Christopher Perkins from UConn are acknowledged for their assistance with FIB/TEM and ICP-OES analysis, respectively. The views and opinions of the authors expressed herein do not necessarily state or reflect those of the United States Government or any agency thereof. Neither the United States Government nor any agency thereof, nor any of their employees, makes any warranty, expressed or implied, or assumes any legal liability or responsibility for the accuracy, completeness, or usefulness of any information,

apparatus, product, or process disclosed, or represents that its use would not infringe privately owned rights.

Reference

(1) Hauch, A.; Kungas, R.; Blennow, P.; Hansen, A. B.; Hansen, J. B.; Mathiesen, B. V.; Mogensen, M. B. Recent advances in solid oxide cell technology for electrolysis. *Science* **2020**, *370* (6513), 186-+. DOI: 10.1126/science.aba6118. Liu, W.; Cui, Y.; Du, X.; Zhang, Z.; Chao, Z. S.; Deng, Y. L. High efficiency hydrogen evolution from native biomass electrolysis. *Energ Environ Sci* **2016**, *9* (2), 467-472. DOI: 10.1039/c5ee03019f.

(2) van Renssen, S. The hydrogen solution? *Nat Clim Change* **2020**, *10* (9), 799-801. DOI: 10.1038/s41558-020-0891-0.

(3) Alves, H. J.; Bley, C.; Niklevicz, R. R.; Frigo, E. P.; Frigo, M. S.; Coimbra-Araujo, C. H. Overview of hydrogen production technologies from biogas and the applications in fuel cells. *Int J Hydrogen Energ* **2013**, *38* (13), 5215-5225. DOI: 10.1016/j.ijhydene.2013.02.057. Holladay, J. D.; Hu, J.; King, D. L.; Wang, Y. An overview of hydrogen production technologies. *Catal Today* **2009**, *139* (4), 244-260. DOI: 10.1016/j.cattod.2008.08.039. Yu, A. S.; Vohs, J. M.; Gorte, R. J. Interfacial reactions in ceramic membrane reactors for syngas production. *Energ Environ Sci* **2014**, *7* (3), 944-953. DOI: 10.1039/c3ee43137a.

(4) Chen, L.; Chen, F. L.; Xia, C. R. Direct synthesis of methane from CO_2-H_2O co-electrolysis in tubular solid oxide electrolysis cells. *Energ Environ Sci* **2014**, *7* (12), 4018-4022. DOI: 10.1039/c4ee02786h.

(5) Park, B. K.; Cox, D.; Barnett, S. A. Effect of Nanoscale $Ce_{0.8}Gd_{0.2}O_{2-\delta}$ Infiltrant and Steam Content on Ni - $(Y_2O_3)_{0.08}(ZrO_2)_{0.92}$ Fuel Electrode Degradation during High-Temperature Electrolysis. *Nano Lett* **2021**, *21* (19), 8363-8369. DOI: 10.1021/acs.nanolett.1c02937.

(6) Shimada, H.; Yamaguchi, T.; Kishimoto, H.; Sumi, H.; Yamaguchi, Y.; Nomura, K.; Fujishiro, Y. Nanocomposite electrodes for high current density over 3 A cm^{-2} in solid oxide electrolysis cells. *Nat Commun* **2019**, *10*. DOI: 10.1038/s41467-019-13426-5.

(7) Sun, X.; Hendriksen, P. V.; Mogensen, M. B.; Chen, M. Degradation in Solid Oxide Electrolysis Cells During Long Term Testing. *Fuel Cells* **2019**, *19* (6), 740-747. DOI: 10.1002/fuce.201900081.

(8) Laguna-Bercero, M. A.; Campana, R.; Larrea, A.; Kilner, J. A.; Orera, V. M. Electrolyte degradation in anode supported microtubular yttria stabilized zirconia-based solid oxide steam electrolysis cells at high voltages of operation. *J Power Sources* **2011**, *196* (21), 8942-8947. DOI: 10.1016/j.jpowsour.2011.01.015. Laguna-Bercero, M. A.; Campana, R.; Larrea, A.; Kilner, J. A.; Orera, V. M. Performance and Aging of Microtubular YSZ-based Solid Oxide Regenerative Fuel Cells. *Fuel Cells* **2011**, *11* (1), 116-123. DOI: 10.1002/fuce.201000069.

(9) Momma, A.; Kato, T.; Kaga, Y.; Nagata, S. Polarization behavior of high temperature solid oxide electrolysis cells (SOEC). *J Ceram Soc Jpn* **1997**, *105* (5), 369-373. DOI: 10.2109/jcersj.105.369. Brichzin, V.; Fleig, J.; Habermeier, H. U.; Cristiani, G.; Maier, J. The geometry dependence of the polarization resistance of Sr-doped $LaMnO_3$ microelectrodes on yttria-stabilized zirconia. *Solid State Ionics* **2002**, *152*, 499-507. Doi 10.1016/S0167-2738(02)00379-X.

(10) Knibbe, R.; Traulsen, M. L.; Hauch, A.; Ebbesen, S. D.; Mogensen, M. Solid Oxide Electrolysis Cells: Degradation at High Current Densities. *J Electrochem Soc* **2010**, *157* (8), B1209-B1217. DOI: 10.1149/1.3447752.

(11) Kim, J.; Ji, H. I.; Dasari, H. P.; Shin, D.; Song, H.; Lee, J. H.; Kim, B. K.; Je, H. J.; Lee, H. W.; Yoon, K. J. Degradation mechanism of electrolyte and air electrode in solid oxide electrolysis cells operating at high polarization. *Int J Hydrogen Energ* **2013**, *38* (3), 1225-1235. DOI: 10.1016/j.ijhydene.2012.10.113.
(12) Shen, F. Y.; Lu, K. Comparative study of $La_{0.6}Sr_{0.4}Co_{0.2}Fe_{0.8}O_3$, $Ba_{0.5}Sr_{0.5}Co_{0.2}Fe_{0.8}O_3$ and $Sm_{0.5}Sr_{0.5}Co_{0.2}Fe_{0.8}O_3$ cathodes and the effect of $Sm_{0.2}Ce_{0.8}O_2$ block layer in solid oxide fuel cells. *Int J Hydrogen Energ* **2015**, *40* (46), 16457-16465. DOI: 10.1016/j.ijhydene.2015.09.148.
(13) Chen, K. F.; Hyodo, J.; Dodd, A.; Ai, N.; Ishihara, T.; Jian, L.; Jiang, S. P. Chromium deposition and poisoning of $La_{0.8}Sr_{0.2}MnO_3$ oxygen electrodes of solid oxide electrolysis cells. *Faraday Discuss* **2015**, *182*, 457-476. DOI: 10.1039/c5fd00010f.
(14) Kim, S. J.; Choi, G. M. Stability of LSCF electrode with GDC interlayer in YSZ-based solid oxide electrolysis cell. *Solid State Ionics* **2014**, *262*, 303-306. DOI: 10.1016/j.ssi.2014.01.001.
(15) The, D.; Grieshammer, S.; Schroeder, M.; Martin, M.; Al Daroukh, M.; Tietz, F.; Schefold, J.; Brisse, A. Microstructural comparison of solid oxide electrolyser cells operated for 6100 h and 9000 h. *J Power Sources* **2015**, *275*, 901-911. DOI: 10.1016/j.jpowsour.2014.10.188.
(16) Shen, F. Y.; Lu, K. Co_3O_4/Sm-Doped CeO_2/Co_3O_4 Trilayer Coating on AISI 441 Interconnect for Solid Oxide Fuel Cells. *ACS Appl Mater Inter* **2017**, *9* (7), 6022-6029. DOI: 10.1021/acsami.6b14562. Shen, F. Y.; Lu, K. Perovskite-type $La_{0.6}Sr_{0.4}Co_{0.2}Fe_{0.8}O_3$, $Ba_{0.5}Sr_{0.5}Co_{0.2}Fe_{0.8}O_3$, and $Sm_{0.5}Sr_{0.5}Co_{0.2}Fe_{0.8}O_3$ cathode materials and their chromium poisoning for solid oxide fuel cells. *Electrochim Acta* **2016**, *211*, 445-452. DOI: 10.1016/j.electacta.2016.06.070.
(17) Sehested, J.; Gelten, J. A. P.; Helveg, S. Sintering of nickel catalysts: Effects of time, atmosphere, temperature, nickel-carrier interactions, and dopants. *Appl Catal A-Gen* **2006**, *309* (2), 237-246. DOI: 10.1016/j.apcata.2006.05.017. Sun, X. F.; Chen, M.; Liu, Y. L.; Hjalmarsson, P.; Ebbesen, S. D.; Jensen, S. H.; Mogensen, M. B.; Hendriksen, P. V. Durability of Solid Oxide Electrolysis Cells for Syngas Production. *J Electrochem Soc* **2013**, *160* (9), F1074-F1080. DOI: 10.1149/2.106309jes.
(18) Lay-Grindler, E.; Laurencin, J.; Villanova, J.; Cloetens, P.; Bleuet, P.; Mansuy, A.; Mougin, J.; Delette, G. Degradation study by 3D reconstruction of a nickel-yttria stabilized zirconia cathode after high temperature steam electrolysis operation. *J Power Sources* **2014**, *269*, 927-936. DOI: 10.1016/j.jpowsour.2014.07.066.
(19) Tucker, M. C. Progress in metal-supported solid oxide fuel cells: A review. *J Power Sources* **2010**, *195* (15), 4570-4582. DOI: 10.1016/j.jpowsour.2010.02.035.
(20) Krishnan, V. V. Recent developments in metal-supported solid oxide fuel cells. *Wires Energy Environ* **2017**, *6* (5). DOI: 10.1002/wene.246.
(21) Tucker, M. C. Progress in metal-supported solid oxide electrolysis cells: A review. *Int J Hydrogen Energ* **2020**, *45* (46), 24203-24218. DOI: 10.1016/j.ijhydene.2020.06.300.
(22) Shen, F. Y.; Wang, R. F.; Tucker, M. C. Long term durability test and post mortem for metal-supported solid oxide electrolysis cells. *J Power Sources* **2020**, *474*. DOI: 10.1016/j.jpowsour.2020.228618.
(23) Shen, F.; Lu, K. Moisture Effect on $La_{0.8}Sr_{0.2}MnO_3$ and $La_{0.6}Sr_{0.4}Co_{0.2}Fe_{0.8}O_3$ Cathode Behaviors in Solid Oxide Fuel Cells. *Fuel Cells* **2015**, *15* (1), 105-114. DOI: 10.1002/fuce.201400032. Ried, P.; Holtappels, P.; Wichser, A.; Ulrich, A.; Graule, T. Synthesis and characterization of La0.6Sr0.4Co0.2Fe0.8O3-delta and $Ba_{0.5}Sr_{0.5}Co_{0.8}Fe_{0.2}O_{3-\delta}$. *J Electrochem Soc* **2008**, *155* (10), B1029-B1035. DOI: 10.1149/1.2960873.
(24) Shen, F. Y.; Lu, K. $La_{0.6}Sr_{0.4}Co_{0.2}Fe_{0.8}O_3$ cathodes incorporated with $Sm_{0.2}Ce_{0.8}O_2$ by three different methods for solid oxide fuel cells. *J Power Sources* **2015**, *296*, 318-326. DOI: 10.1016/j.jpowsour.2015.07.060.
(25) Wang, C. C.; Gholizadeh, M.; Hou, B. X.; Fan, X. C. Integrated Cr and S poisoning of a $La_{0.6}Sr_{0.4}Co_{0.2}Fe_{0.8}O_{3-\delta}$ (LSCF) cathode for solid oxide fuel cells. *RSC Adv* **2021**, *11* (1), 7-14. DOI: 10.1039/d0ra09239h.

(26) Reisert, M.; Berova, V.; Aphale, A.; Singh, P.; Tucker, M. C. Oxidation of porous stainless steel supports for metal-supported solid oxide fuel cells. *Int J Hydrogen Energ* **2020**, *45* (55), 30882-30897. DOI: 10.1016/j.ijhydene.2020.08.015.
(27) Mah, J. C. W.; Muchtar, A.; Somalu, M. R.; Ghazali, M. J. Metallic interconnects for solid oxide fuel cell: A review on protective coating and deposition techniques. *Int J Hydrogen Energ* **2017**, *42* (14), 9219-9229. DOI: 10.1016/j.ijhydene.2016.03.195.
(28) Sun, Z. H.; Wang, R. F.; Nikiforov, A. Y.; Gopalan, S.; Pal, U. B.; Basu, S. N. $CuMn_{1.8}O_4$ protective coatings on metallic interconnects for prevention of Cr-poisoning in solid oxide fuel cells. *J Power Sources* **2018**, *378*, 125-133. DOI: 10.1016/j.jpowsour.2017.12.031.
(29) Zhu, Z. K.; Pal, U.; Gopalan, S.; Hussain, A. M.; Dong, S.; Dale, N.; Fukuyama, Y.; Basu, S. Alternating-Current Electrophoretic Deposition of Spinel Coatings on Porous Metallic Substrates for Solid Oxide Fuel Cell Applications. *Jom-Us* **2021**, *73* (9), 2764-2770. DOI: 10.1007/s11837-021-04763-2.
(30) Dogdibegovic, E.; Wang, R. F.; Lau, G. Y.; Karimaghaloo, A.; Lee, M. H.; Tucker, M. C. Progress in durability of metal-supported solid oxide fuel cells with infiltrated electrodes. *J Power Sources* **2019**, *437*. DOI: 10.1016/j.jpowsour.2019.226935.
(31) Wang, R. F.; Sun, Z. H.; Pal, U. B.; Gopalan, S.; Basu, S. N. Mitigation of chromium poisoning of cathodes in solid oxide fuel cells employing CuMn1.8O4 spinel coating on metallic interconnect. *J Power Sources* **2018**, *376*, 100-110. DOI: 10.1016/j.jpowsour.2017.11.069.
(32) Dogdibegovic, E.; Cheng, Y.; Shen, F. Y.; Wang, R. F.; Hu, B. X.; Tucker, M. C. Scaleup and manufacturability of symmetric-structured metal-supported solid oxide fuel cells. *J Power Sources* **2021**, *489*. DOI: 10.1016/j.jpowsour.2020.229439.
(33) Wang, R. F.; Sun, Z. H.; Choi, J. P.; Basu, S. N.; Stevenson, J. W.; Tucker, M. C. Ferritic stainless steel interconnects for protonic ceramic electrochemical cell stacks: Oxidation behavior and protective coatings. *Int J Hydrogen Energ* **2019**, *44* (47), 25297-25309. DOI: 10.1016/j.ijhydene.2019.08.041.
(34) Wei, B.; Chen, K. F.; Zhao, L.; Lu, Z.; Jiang, S. P. Chromium deposition and poisoning at La0.6Sr0.4Co0.2Fe0.8O3-delta oxygen electrodes of solid oxide electrolysis cells. *Phys Chem Chem Phys* **2015**, *17* (3), 1601-1609. DOI: 10.1039/c4cp05110f.

Table of contents